BARS AND COLD DARK MATTER HALOS

Pedro Colín

Centro de Radiostronomía y Astrofísica, Universidad Nacional Autónoma de México, Apartado Postal 72-3 (Xangari),
58089 Morelia, Michoacán, Mexico

O. Valenzuela

Department of Astronomy, Box 351580, University of Washington, Seattle, WA 98195-1580

and

A. Klypin

Department of Astronomy, Box 30001, Department 4500, New Mexico State University, Las Cruces, NM 88003-0001

ABSTRACT

The central part of a dark matter halo reacts to the presence and evolution of a bar. Not only does the halo absorb angular momentum from the disk, it can also be compressed and have its shape modified. We study these issues in a series of cosmologically motivated, highly resolved N-body simulations of barred galaxies run under different initial conditions. In all models we find that the inner halo's central density increases. We model this density increase using the standard adiabatic approximation and the modified formula by Gnedin et al., and we find that halo mass profiles are better reproduced by the latter. In models with a strong bar, the dark matter in the central region forms a barlike structure ("dark matter bar"), which rotates together with the normal bar formed by the stellar component ("stellar bar"). The minor-to-major axial ratio of a halo bar changes with radius with a typical value 0.7 in the central disk region. Dark matter bar amplitude is mostly a function of the stellar bar strength. For models in which the bar amplitude increases or stays roughly constant with time, initially large ($40°–60°$) misalignment between the halo and disk bars quickly decreases with time as the bar grows. The halo bar is nearly aligned with the stellar bar ($\sim 10°$ lag for the halo) after ~ 2 Gyr. The torque, which the halo bar exerts on the stellar bar, can serve as a mechanism to regulate the angular momentum transfer from the disk to the halo.

Subject headings: galaxies: evolution — galaxies: halos — galaxies: kinematics and dynamics —
                  methods: n-body simulations

Online material: color figures

1. INTRODUCTION

The cold dark matter scenario for galaxy formation predicts that galaxies should be embedded within massive, extended, hot, and cuspy dark matter halos. The halos can have as much as 20 times more mass than the disk. They extend well beyond the visible galaxy. Halos are hot because they are supported against gravity by a large velocity dispersion. Halos are cuspy because their central density profiles go as $r^{-\alpha}$, with $\alpha \sim 1.0$. Unfortunately, for historical reasons,[1] for simplicity, and because of a lack of computer resources, most studies of stellar bars have assumed unrealistic halos, from rigid ones (papers in the 1970s, with few exceptions) to live but small ones (papers in the 1980s and 1990s). The need for a realistic halo component is being recognized, and nowadays models in which this dark component satisfies some or all of the above requirements are more commonly found in the literature (Debattista & Sellwood 2000; Athanassoula 2003; Valenzuela & Klypin 2003; O'Neill & Dubinski 2003; Holley-Bockelmann et al. 2005).

A *systematic* study of the structural and dynamical changes that the dark matter (DM) component experiences in the presence and during the evolution of a bar is missing. Most studies that address the issue have focused on the angular momentum transfer from the bar to the halo (e.g., Weinberg 1985; Combes et al. 1990; Little & Carlberg 1991; Hernquist & Weinberg 1992; Athanassoula 1996; Debattista & Sellwood 2000). For example, Weinberg (1985) and Hernquist & Weinberg (1992), using rigid bars, found that a bar loses its angular momentum in a few rotation periods because of the dynamical friction that the dark matter exerts on it. This angular momentum transfer flattens out the initially cuspy halo density profile (see also Holley-Bockelmann et al. 2005).

There is no doubt that the disk loses angular momentum due to this transfer mechanism, but the amount and the rate at which this happens is still a matter of debate. Fully self-consistent N-body simulations with live disk and dark matter halos (e.g., Athanassoula 1996; Debattista & Sellwood 1998, 2000; Athanassoula & Misiriotis 2002; Valenzuela & Klypin 2003) show that bars slow down far less than those predicted by Weinberg (1985) and Hernquist & Weinberg (1992). Debattista & Sellwood (1998, 2000) find in their massive halo models, i.e., those for which the contributions of the disk and the halo to the mass in the central region are comparable, that the disk loses about 40% of its initial angular momentum in ~ 10 Gyr. During this time interval the bar pattern speed, Ω_p, decreases by a factor of 4. Valenzuela & Klypin (2003), in simulations with much better force resolution and a more realistic cosmological halo setup, find a decrease in Ω_p of only a factor of 2 in ~ 7 Gyr (see their model A_2).

The response of the DM halo to the transfer of the stellar material from the middle parts of the disk closer to the center has recently been studied by Holley-Bockelmann et al. (2005) and

---

[1] A well-established *galactic-scale* cold dark matter cosmology did not arise until the late-1990s.

Sellwood (2003) in relation to the *cuspy* problem. Cosmology predicts cuspy inner density profiles that appear to disagree with those derived from rotation curves of dwarf and low surface brightness galaxies (e.g., de Blok et al. 2003; Weldrake et al. 2003; but see also Swaters et al. 2003; Rhee et al. 2004). Holley-Bockelmann et al. (2005) find a decrease in the halo central density, while simulations by Sellwood (2003) show the contrary. Here we discuss halo density profiles within the context of adiabatic approximation models (e.g., Blumenthal et al. 1986; Ryden & Gunn 1987; Gnedin et al. 2004). Do dark matter halos respond to the increase of stellar mass in the center by contracting? If so, can this increase in density be modeled by the standard adiabatic approximation? In agreement with Sellwood (2003), we show that in our models the halo central density increases, sometimes by as much as a factor of 3.

The influence of the bar on the morphology of a halo or a spheroid is a point that has only been touched on briefly in the literature. Yet it is an issue that deserves a more detailed analysis. It may be important for accurate testing of cosmological predictions, which are becoming a reality (e.g., Ibata et al. 2001). For example, in our bar models we find that the initially spherical halo flattens to values comparable to those found in cosmological halos, for which the minor-to-major axial ratio s is $s \approx 0.7$ (e.g., Jing & Suto 2002). This correlation between the morphology of the stellar component and that of the DM halo has also been seen in cosmological gasdynamic simulations of galaxies (Kazantzidis et al. 2004).

Returning to bar simulations, Combes et al. (1990) found no significant flattening of the bulge particles ($s \approx 1$) in their experiment A, for which $M_b/M_d = 0.5$, where M_b and M_d are the mass of the bulge and the disk, respectively. Debattista & Sellwood (2000) studied the halo response to the bar by measuring the second harmonic of the angular DM particle distribution and found that the phase difference between the disk and the halo bar gradually goes to zero. This effect was also seen in the simulations by O'Neill & Dubinski (2003): after $t \sim 10$ Gyr the orientations of bars (halo and disk) stay within $10°$ of one another. The halo bar found by O'Neill & Dubinski (2003) was not very elongated. The axial ratio was only 0.88. Halo bars have also seen by Holley-Bockelmann et al. (2005; see their Fig. 2) and Athanassoula (2005a, 2005b). Based on results of simulations with strong bars, Athanassoula (2005a, 2005b) finds that halo bars are prolate-like, with inner axial ratios being 0.7 or 0.8.

More recently, in order to understand the role of the halo in the formation and evolution of the bar, Athanassoula (2002, 2003) has carried out an orbital-resonant study of the disk and halo particles in models in which the disk parameters are kept fixed while varying the degree of the halo influence. She found significant differences in the halo orbital properties between her halo and disk-dominated models. The inner Lindblad resonance (ILR) is present in the halo-dominated models, while in the disk-dominated ones it is not. In general, she found that there is much more material between the ILR and corotation in the former models than in the latter ones. Because these halo-dominated models have stronger bars than their counterparts, disk-dominated ones, this result shows the positive effect that a live halo has on the bar growth.

The paper is organized as follows: In § 2 we introduce the models to be explored in this paper. In § 3 we present the evolution of the amplitude and pattern speed of the bar. Section 4 is devoted to an analysis of models of adiabatic compression, which are used in the context of the inner disk density growth. The influence of the disk and stellar bar on the initially spherically symmetric halo is discussed in § 5. In particular, we show that once formed, the halo bar tends to rapidly align with the stellar bar. A

brief discussion of the redistribution and evolution of the disk angular momentum is given in § 6. In § 7 we discuss our results and summarize our main conclusions.

2. MODELS AND SIMULATIONS

2.1. *Initial Conditions*

The initial conditions are described in Valenzuela & Klypin (2003). Here we briefly summarize parameters of our models. The system of a halo and a disk, with no initial bulge or a bar, is generated using the method of Hernquist (1993). In cylindrical coordinates the density of the stellar disk is approximated by the following expression:

$$\rho_d(R, z) = \frac{M_d}{4\pi z_0 R_d^2} e^{-R/R_d} \text{sech}^2(z/z_0), \quad (1)$$

where M_d is the mass of the disk, R_d is the scale length, and z_0 is the scale height. The latter is assumed constant through the disk. The radial and vertical velocity dispersion are given by

$$\sigma(R) = Q \frac{3.36 G\Sigma(R)}{\kappa(R)}, \quad \sigma_z^2(R) = \pi G z_0 \Sigma(R), \quad (2)$$

where κ is the epicyclic frequency and Q is the stability or Toomre parameter. Our models keep Q fixed along the disk. The azimuthal velocity and its dispersion are found using the asymmetric drift and the epicycle approximations.

The models assume a Navarro-Frenk-White (NFW) density profile (Navarro et al. 1997) for the halo component, which is described by

$$\rho_{\text{DM}}(r) = \frac{\rho_0}{x(1+x)^2}, \quad x \equiv r/r_s, \quad (3)$$

$$M_{\text{vir}} = 4\pi\rho_0 r_s^3 \left[\ln(1+c) - \frac{c}{1+c} \right], \quad c = \frac{R_{\text{vir}}}{r_s}, \quad (4)$$

where M_{vir}, R_{vir}, and c are the virial mass, the virial radius, and concentration of the halo, respectively. Given M_{vir}, the virial radius is found once a cosmology is adopted.[2] Equations (4–56) of Binney & Tremaine (1987) and the assumption of isotropy in the velocities allow us to determine the radial velocity dispersion as

$$\sigma_{r,\text{DM}}^2 = \frac{1}{\rho_{\text{DM}}} \int_r^\infty \rho_{\text{DM}} \frac{GM(r)}{r^2} dr, \quad (5)$$

where $M(r)$ is the mass contained within radius r and G is the gravitational constant.

The dark matter halo is truncated at the virial radius, which for our D and K models is 287 kpc, while for our A_{wb} model it is 323 kpc (see Table 1). The disk component is realized with particles of equal mass. The halo is composed of particles of different mass placed inside out as we go from less to more massive particles. The smallest particles have a mass equal to those of the disk. The multiple-mass scheme is designed to reduce the total number of particles and thus the CPU time.

Parameters of our models are presented in Table 1. They were chosen to cover a relatively wide range of the parameter space:

---

[2] We adopt the flat cosmological model with a nonvanishing cosmological constant with $\Omega_0 = 0.3$ and $h = 0.7$.

Parameter	A_{wb}	D_{cs}	D_{cb}	D_{hs}	K_{cb}	K_{wb}	K_{hb}
Disk mass ($10^{10} M_\odot$)...	4.28	5.0	5.0	5.0	5.0	5.0	5.0
Total mass ($10^{12} M_\odot$)	2.04	1.43	1.43	1.43	1.43	1.43	1.43
Disk exponential length R_d (kpc)	3.50	2.57	3.86	2.57	3.86	3.86	3.86
Disk exponential height z_0 (kpc)	0.14	0.20	0.20	0.20	0.20	0.20	0.20
Toomre parameter Q	1.6	1.3	1.3	1.8	1.2	1.5	1.8
Halo concentration C	15	17	17	17	10	10	10
Number of disk particles (10^5)	2.0	2.33	2.33	4.60	2.33	2.33	2.33
Total number of particles (10^6)	2.7	2.5	1.9	3.80	2.3	2.7	2.3
Particle mass ($10^5 M_\odot$)	2.14	1.07	2.14	1.07	2.14	2.14	2.14
Time step (10^4 yr)	1.5	2.0	1.5	1.5	1.2	1.5	2.0
Minimum cell size (pc)	22	48	22	22	24	22	48
Disk-to-DM mass ratio inside R_d	0.82	2.03	0.98	2.03	1.95	1.95	1.95
Strong bar after 5 Gyr ($A_2 > 0.4$).............................	yes	yes	yes	no	no	no	no

there are hot and cold models, K_{hb} versus K_{cb}; there is a disk-dominated D_{cs} and a submaximum D_{cb} model. There are models with different DM halo concentrations: D_{cb} and K_{cb}. The parameter values are similar to those used by Valenzuela & Klypin (2003), whose models were chosen to mimic the properties of the Milky Way (Klypin et al. 2002). More specifically, models labeled with D all have the same disk mass, total mass, and halo concentration. The halo concentration is above the median ~13 for a halo of the mass and cosmology adopted here (Bullock et al. 2001). On the other hand, models K differ from one another only by the value of the disk stability parameter Q.

As a measure of the density of the halo in the central region, we show in Table 1 the disk-to-DM mass ratio evaluated at the disk exponential length R_d. The values are about 1−2. In other words, from the beginning, the dark matter is subdominant in the central region. This is broadly consistent with the mass modeling of the Milky Way (Klypin et al. 2002): even for cosmologically motivated cuspy DM halos, the density of the dark matter must be smaller than the density of the baryons in the central region of galaxies. This is different from what is often assumed in simulations of barred galaxies. For example, in the DM-dominated models of Athanassoula & Misiriotis (2002) the halo mass dominates everywhere inside $2R_d$. This is not consistent with cosmological predictions. We do allow variations of the DM mass in the central region. For example, model D_{cb} has a denser halo than models K. Models D_{cb} and A_{wb}, in which initially the disk is less dominant, develop strong bars. The last row of Table 1 classified the models according to stellar bar strength after 5 Gyr of evolution. We label them as strong bar models if they develop a bar with an amplitude A_2 larger than 0.4.

Figure 1 shows the initial circular velocities profiles $V_c = [GM(r)/r]^{1/2}$ for all the components. This estimate of V_c assumes spherical symmetry. The circular velocity estimated in the plane of the disk using the real nonspherical distribution $V_{c,z=0} \equiv [g(r)r]^{1/2}$, where $g(r)$ is the gravitational acceleration in the disk plane, is very close (within 5%) to the circular velocity V_c at radii larger than 1 kpc. At smaller distances it is slightly (10%−20%) *below* V_c.

2.2. Numerical Simulations

The simulations were run with the adaptive refinement tree (ART) code (Kravtsov et al. 1997). The ART code starts with a uniform grid, which covers the whole computational box. This grid defines the lowest (zeroth) level of resolution of the sim-

ulation. Two grids with 256^3 and 128^3 cells in the zeroth level and boxes of 1.43 and 1.0 Mpc across, respectively, were used by the simulations presented here. The models are placed at the center of the grid and far from the periodic images. Because the size of the models are small compared with the box sizes, the effects of the periodical images are negligible. For example, at a distance of 100 kpc from the center of a model, in the 1.43 Mpc box, the relative contribution of periodic images is less that 7×10^{-7} of the main galaxy force. Even at 250 kpc, which is close to the virial radius for the models, the tidal force is only 6×10^{-5} of the force from the central image. Bar formation and evolution are practically unaffected by the periodic boundary conditions.

The ART code achieves high spatial resolution by refining the base uniform grid in all high-density regions with an automated refinement algorithm. The standard cloud-in-cell algorithm is used to compute the density and gravitational potential on the zeroth-level mesh with periodical boundary conditions. The code then reaches high force resolution by refining all high-density regions using an automated refinement algorithm. The refinements are recursive. A refined region can also be refined. Each subsequent refinement level has half of the previous level's cell size. This creates a hierarchy of refinement meshes of different resolution, size, and geometry covering regions of interest. Because each individual cubic cell can be refined, the shape of the refinement mesh can be arbitrary and effectively match the geometry of the region of interest. This algorithm is well suited for simulations of a selected region within a large computational box, as in the simulations presented below.

The criterion for refinement is the local density of particles. If the number density of particles in a mesh cell (as estimated by the cloud-in-cell method) exceeds the level n_{thresh}, the cell is split ("refined") into eight cells of the next refinement level. The refinement threshold depends on the refinement level. The threshold for cell refinement was low on the zeroth level: $n_{thresh}(0) = 2$. Thus, every zeroth-level cell containing two or more particles was refined. The threshold was higher on deeper levels of refinement: $n_{thresh} = 3$ and 4 for the first level and higher levels, respectively. Note that the code actually does not count the number of particles in a cell to decide whether the cell should be split or not. It uses the density field, which is less noisy than counting particles. It then filters the density field to make the map of refinement even smoother. On average, the algorithm maintains 1−4 particles per cell. Yet some cells have few particles in them, and some can
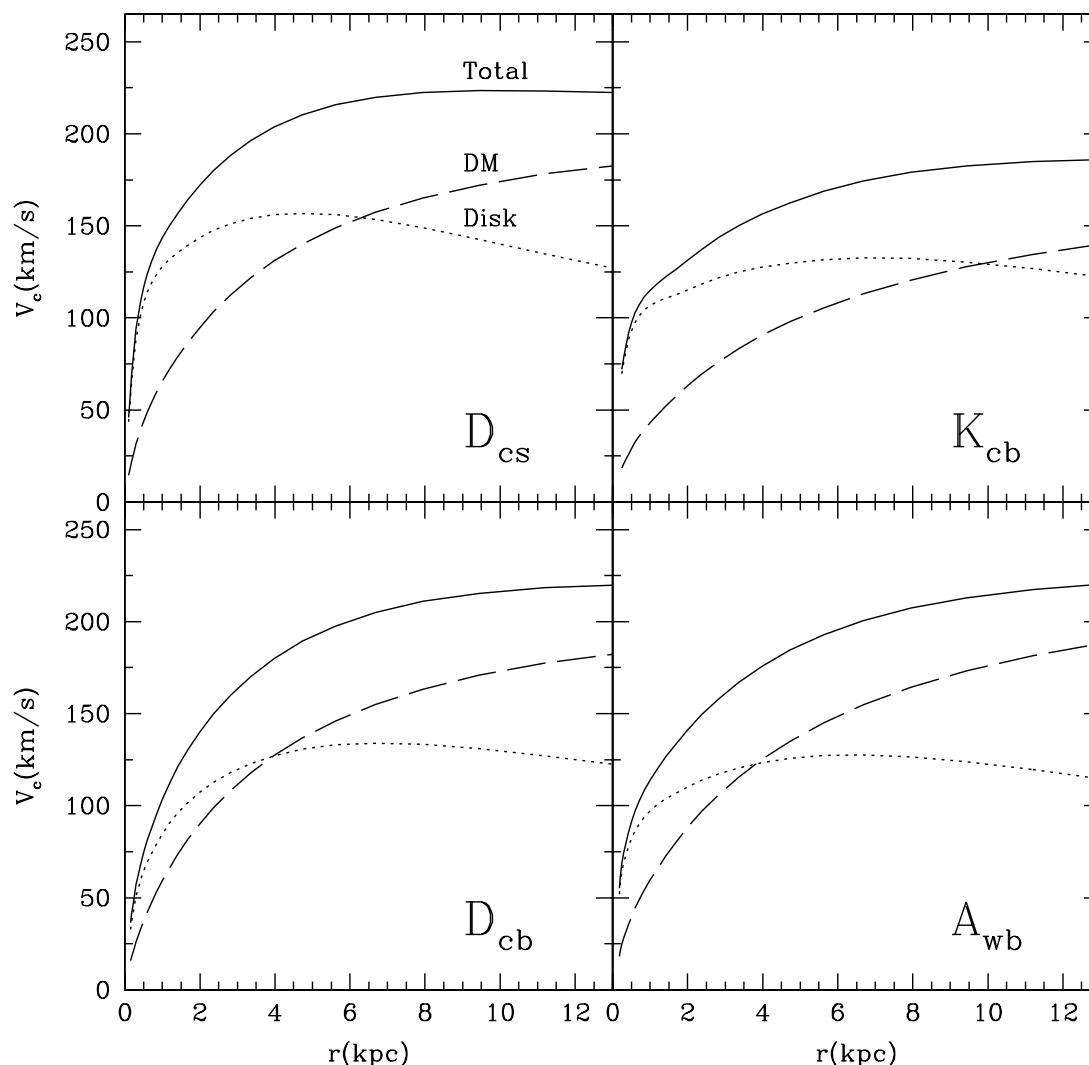
Fig. 1.—Initial circular velocities profiles for models D_{cs} and K_{cb} (*top*) and D_{cb} and A_{wb} (*bottom*). Total, stellar, and halo components are denoted by solid, dotted, and dashed lines, respectively. In the disk-dominated models (*top*) the system evolves secularly, producing a weak bar at later stages, while in the halo-dominated models (*bottom*) a strong bar is present after 5 Gyr of evolution. [*See the electronic edition of the Journal for a color version of this figure.*]

even be empty. Those cells are not used for estimates of the gravitational acceleration acting on particles. For each particle the code checks whether all 56 cells surrounding the cell hosting the particle are on the same level of refinement. If they are not, then the code assigns the particle to a lower resolution and checks again for the refinement level of all its neighbors. In two of our models (D_{cs} and K_{hb}) we limited the resolution to not more than seven levels of refinement.

The resolution changes from place to place, and it also changes with time. During the initial stage of evolution—the formation of the bar—the density in the central part increases substantially. For example, in model K_{cb} the density at 250 pc increases by a factor of 10 by the end of the evolution. The code reacts to this density increase by changing the number of high-resolution cells. The lion's share of this increase happens during the first 0.5 Gyr when the system develops very strong nonaxisymmetric fluctuations. For example, in the case of model K_{cb} the density at the central 250 pc increases 6 times during the first $t = 0.5$ Gyr. It will take another 5 Gyr to double it. The code increases the number of high-resolution 24 pc cells 14 times during the first 0.5 Gyr of evolution. The number of cells then changes only by 30% during the remaining 5 Gyr. The increase on lower 48 pc level of

resolution is even smaller: the number of cells increased only by 20% during the whole evolution. Note that this implies that the size of the high-resolution region changes only by 6%. In other words, the increase of the resolution with time is very mild, and most of it happens before the bar forms and settles.

The spatial resolution varies with the distance. Typically in the models the central roughly elliptical region with large axis 1.5 kpc (4 kpc) is resolved with 20–25 pc cells (40–50 pc). The whole disk (up to radius of about 15 kpc) is resolved with 80–100 pc cells. The force resolution in our simulations is 2 times larger than a cell size. Inside one resolution element (roughly a sphere of two cell radii) the code has, on average, 64 particles. This large number of particles implies that the code does not produce too high a resolution for the number of particles present in our models. The effect of close encounters is actually even smaller than what it seems from naive counting particles. The natural scale of the close encounters is Chandrasekhar's minimum impact parameter $b_{min} = Gm/V^2$, which is the distance for 90° deflection (here m is the particle mass and V is the relative velocity). One does not want to get close to it, but it still gives a scale for the small-distance scattering. In the central 1 kpc region of our models the rms velocity of particles is about 200 km s^{-1}. With the mass of
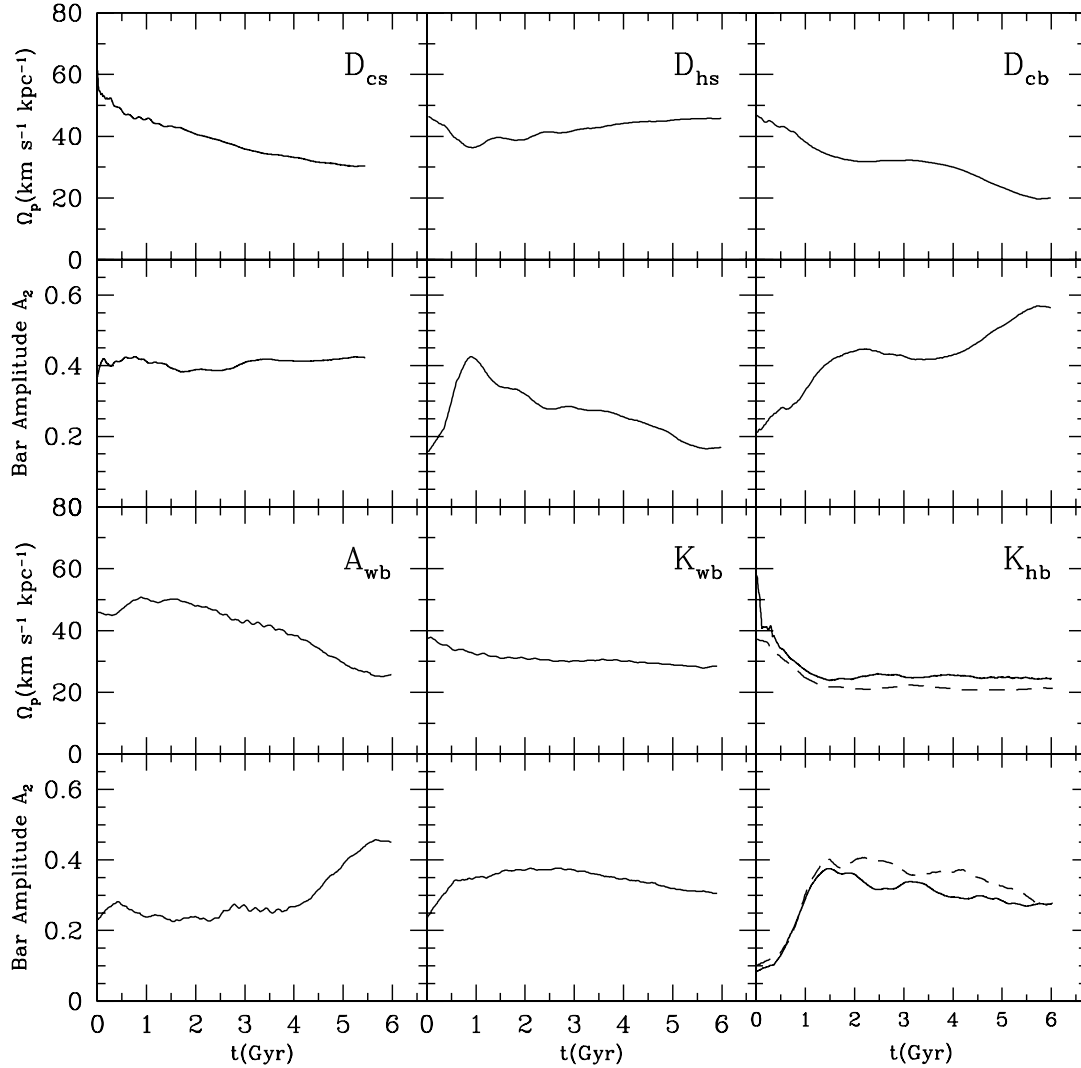
Fig. 2.—Evolution of the bar pattern speed (*first and third rows*) and the bar amplitude (*second and fourth rows*) for six of our seven models. Models D_{cs}, K_{wb}, and K_{hb} evolve very slowly after the bar formation. In models D_{hs} and K_{cb} (not shown in the plot), the bar amplitude, after reaching a peak, decreases as a function of time. In models A_{wb} and D_{cb}, at late stages of the evolution, the bar develops a second growth period. The dashed curves in the K_{hb} model show results obtained with the GADGET code.

a particle of $2 \times 10^5 \ M_\odot$, we get $b_{min} = 2 \times 10^{-2}$ pc. This is 2000 times smaller than our resolution of 50 pc. And this still overestimates the effect because we have many particles inside the resolution element. At larger distance, say 5 kpc, the rms velocity in the disk is smaller. Again, taking a typical rms velocity from our models, we get $b_{min} = 0.1$ pc. With the cell size of 88 pc (resolution 160 pc) we are still 2000 times away from b_{min}. To summarize, the effects of close collisions are definitely small in our models.

During the integration, spatial refinement is accompanied by temporal refinement. Namely, particles moving on each level of refinement are advanced using the leap-frog scheme. When a particle moves to another level, its velocity is reinterpolated. The time step decreases by a factor of 2 with each refinement level. This variable time stepping is very important for the accuracy of the results. As the force resolution increases, more steps are needed to integrate the trajectories accurately.

2.3. *Code Tests*

ART code has been extensively tested during the last ~10 years. A list of tests and details are presented in Valenzuela & Klypin (2003). Here we give a brief summary of those that are

important for our problems. Among other tests, Kravtsov et al. (1997) tested the code using the spherical accretion model. A small initial seed is placed in a homogeneous expanding background. Shells surrounding the seed start to accrete on the seed, which results in the buildup of a very centrally concentrated object. An analytical solution for this complicated process is known (the Bertschinger solution). In the test, the density increases by almost 5 orders of magnitude. At the end, no detectable deviations of the numerical solution provided by ART and the analytical solution were found. This is an important test because it shows that the code accurately treats collapsing systems. In the simulations of barred galaxies, this collapse happens during the initial stage of formation of bars (first ~1 Gyr of evolution), when the density in the central region increases few times. Asymmetric collapse was tested (Kravtsov et al. 1997) using the Zel'dovich approximation (plane wave collapse).

Valenzuela & Klypin (2003) present additional tests, which focus on a long-term stability of equilibrium systems. These tests are relevant for later stages of evolution of barred models, when the system changes its structure very gradually. Valenzuela & Klypin (2003) used 200,000 particles to set equilibrium for a high-concentration NFW halo. The test is actually very difficult

for the code. Orbits of particles in the NFW halo are very elongated. Thus, particles move again and again from high-density regions with high force resolution to outer regions with low resolution and back. Any numerical defects at boundaries of regions of different resolution would result in evolution of the system or in excessive scattering of trajectories. No defects were detected for gigayears of evolution. Using trajectories of individual particles, Valenzuela & Klypin (2003) estimated effects of the two-body scattering in the simulations. The two-body scattering is clearly present. It is consistent with predictions of the Chandrasekhar approximation (after some scaling due to inhomogeneous distribution of density). Yet the time for the two-body scattering is very long: for a typical run with 3×10^6 particles the two-body relaxation time is $\approx 4 \times 10^4$ Gyr. So it is practically negligible.

Numerical two-body scattering is often discussed in conjunction with effects of resonances in barred galaxies (e.g., Weinberg & Katz 2005). Excessive scattering may prevent accurate treatment of resonances, which are important factors in disk galaxies. Formation of bars in dark matter, discussed below, is an example of resonant interaction between stellar bars and the dark matter. D. Ceverino & A. Klypin (2006, in preparation) studied resonances in some of our models. A large number of strong resonances were detected, including the familiar corotation and the inner and outer Lindblad resonances. Thus, the two-body scattering in our simulations is small enough for the resonance to be present and to be a very important factor in the evolution of the systems.

After reaching a peak in their amplitude, bars in our models can grow, gradually decline, or remain in a steady state with little change in the amplitude. For models with relatively low central densities (e.g., A_{wb} and K_{hb}) the evolution with time is robust against changes of the numerical parameters: the time step, the number of the particles, and the force resolution. We rerun some of our models, doubling the number of particles while keeping the same *small* time step, and the results do not change significantly. We also run the K_{hb} model with the GADGET code (Springel et al. 2001). In this case we used only 10^5 particles in the disk and 10^6 total. The force resolution was limited to 100 pc (Plummer softening). At the beginning of the simulation the time step was $\sim 1.5 \times 10^5$ yr, while by the end of the evolution it had reduced to $\sim 4.4 \times 10^4$ yr. Figure 2 shows the evolution of the pattern speed Ω_p and the bar amplitude A_2 for model K_{hb} run with the GADGET and the ART codes. Overall, the agreement with the ART code is reasonably good. After 5 Gyr of evolution the bar amplitudes and the bar lengths are within 10%. The pattern speeds deviate not more than 20%. Note that both simulations of the K_{hb} model show the same qualitative behavior: the pattern speed is barely changing over 5 Gyr of evolution, and the amplitude of the bar is gradually decreasing with time.

3. THE BAR PATTERN SPEED

Figure 2 shows the evolution of the bar pattern speed Ω_p and the amplitude of the bar A_2 for six models. To estimate Ω_p we first determine the orientation of the bar computed applying iteratively the method of the tensor of inertia in the plane of the disk (see § 5 below). Parameter Ω_p is obtained subsequently by numerical differentiation: $\Omega_p = d\phi/dt$, where ϕ is the position angle of the bar. In practice, we use about 10 consecutive snapshots for which the increasing function ϕ is available and make a least-squares fit. Then Ω_p is given by the slope of the straight line. The bar amplitude A_2 is computed as in Valenzuela & Klypin (2003). The curves are smoothed out in time by using a top-hat kernel. Models show what seems to be a generic feature of bar
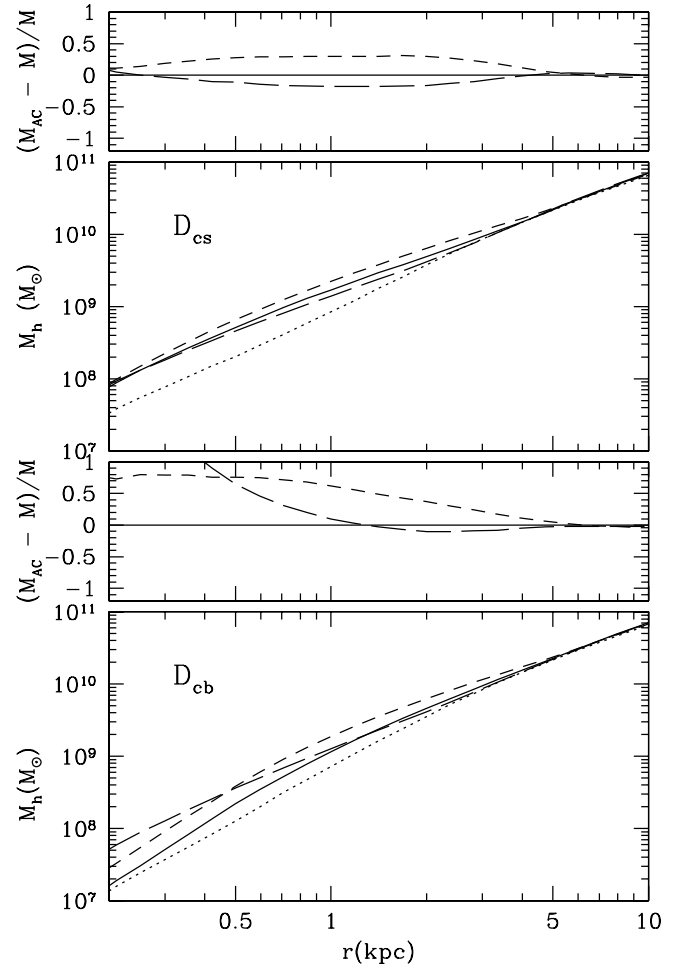

FIG. 3.—Cumulative halo mass profiles for models D_{cs} and D_{cb}. Initial profiles are shown by dotted curves. The profile at the last simulated epoch $t \sim 6$ Gyr is presented using full curves. Results of the standard and the modified adiabatic approximations are presented with short-dashed and long-dashed curves. In the small panels we also show the relative mass differences between the adiabatic approximations and the mass profiles as measured in simulations. [*See the electronic edition of the Journal for a color version of this figure.*]

simulations: an increase in A_2 is accompanied with a decline in Ω_p and vice versa. A steady amplitude, on the other hand, produces a roughly constant Ω_p.

4. ADIABATIC CONTRACTION

The structure and the dynamics of the halo is altered by the presence and evolution of the disk and vice versa. For example, the halo's inner shape changes from the assumed initial spherical configuration to a triaxial one. We see that in models in which a strong bar develops, the halo becomes prolate. The $m = 2$ structure of the halo, the DM bar, which arises because of the bar instability of the disk, couples with the stellar bar. It is an important contributor to the stellar bar braking (see § 6 below). In this section, we study the changes in its mass structure.

It is known (e.g., Athanassoula & Misiriotis 2002; Valenzuela & Klypin 2003; Avila-Reese et al. 2005) that as the stellar bar grows, the inner disk density increases. Is this density growth accompanied with a corresponding central halo mass increase? If so, can it be modeled by the standard adiabatic contraction approximation? This latter model assumes spherical symmetry, homologous contraction, particles in circular orbits, and conservation
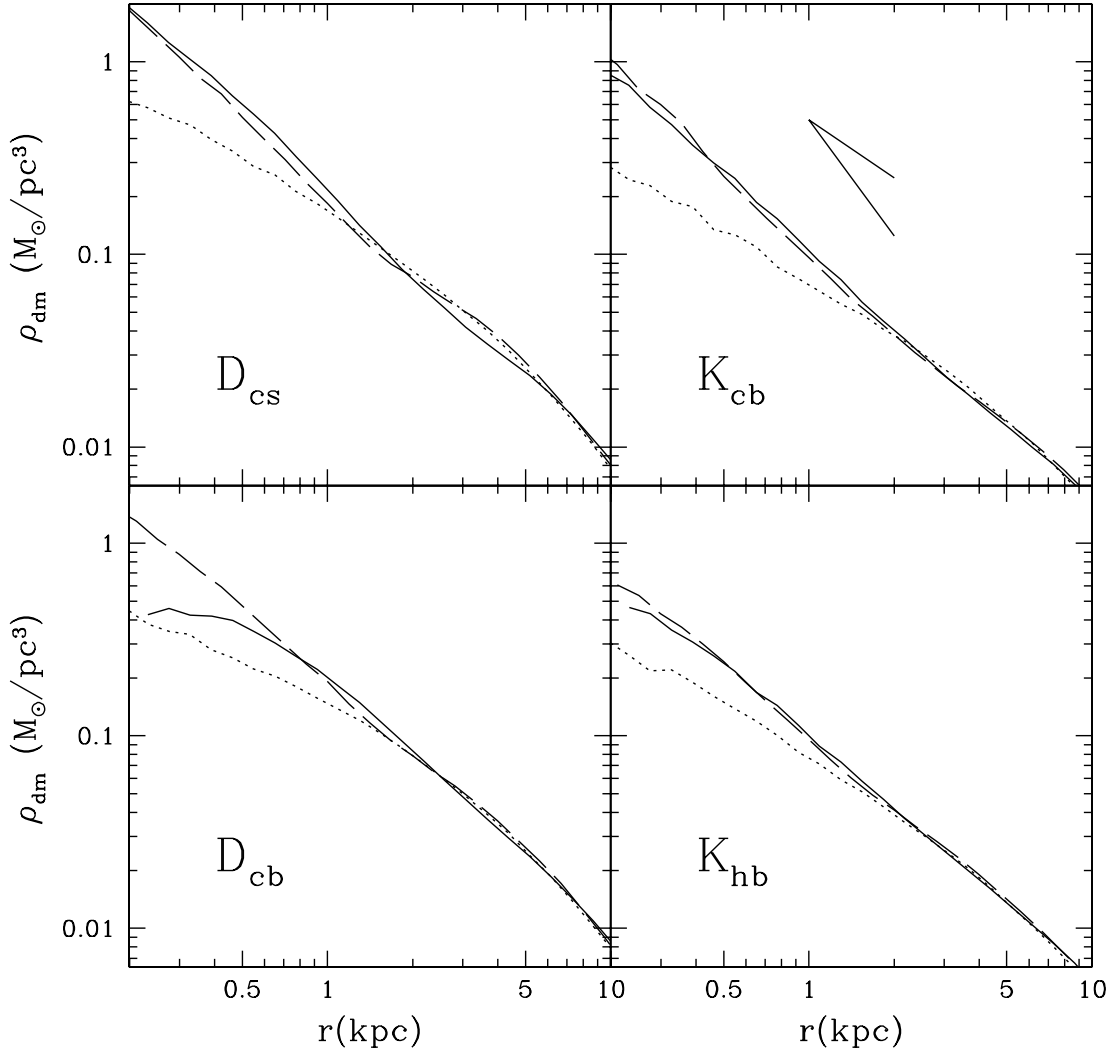
Fig. 4.—Spherically averaged DM density profiles for models D_{cb}, K_{hb}, D_{cs}, and K_{cb}. Curves are coded as in Fig. 3: initial profile (*dotted curve*), the profile at the end of the evolution, $t \sim 6$ Gyr, (*solid curve*), and the adiabatic approximation of Gnedin et al. (*long-dashed curve*). Noise in initial and final density profiles was reduced by averaging five consecutive time steps. For comparison, in the top right panel we show power laws with the slope -1 and -2. [*See the electronic edition of the Journal for a color version of this figure.*]

of the angular momentum (Blumenthal et al. 1986; Ryden & Gunn 1987; Gnedin et al. 2004). Under these assumptions, the final halo cumulative mass profile can be computed given the initial DM and baryonic mass profiles, $M_{DM}(r)$, $M_b(r)$, and the final baryonic profile, $M_b(r_f)$:

$$[M_{DM}(r) + M_b(r)]r = [M_{DM}(r) + M_b(r_f)]r_f. \qquad (6)$$

Given r_f and thus $M_b(r_f)$, we solve the above equation for r iteratively. The initial mass profiles as well as the final baryonic profiles are taken from simulations. To reduce noise, both final and initial profiles are smoothed out over a few close time steps. Gnedin et al. (2004) recently tested the model in cosmological simulations and found that it systematically overestimates the central density. Note that since the orbits of DM particles are on average eccentric, the assumption of circular orbits of the standard formalism breaks. Gnedin et al. (2004) show that the model can be improved if the adiabatic invariant is changed from $M(r)r$ to $M(\bar{r})r$, where r and $\bar{r}$ are the current and orbit-averaged particle positions, respectively. This modification approximately ac-

counts for the eccentricity of particle orbits. It was found that $\bar{r}$ can be described by a power law:

$$\bar{x} = Ax^w, \qquad x \equiv r/r_{vir}, \qquad (7)$$

with small variations in the A and w parameters. We test the new model, adopting mean values given by Gnedin et al. (2004): $A = 0.85$ and $w = 0.8$.

Figure 3 shows the initial and the final halo mass profiles for models D_{cs} (*top panel*) and D_{cb} (*bottom panel*). The mass profile in model D_{cb} barely changes, while in model D_{cs} the mass at 0.5 kpc, for example, has increased substantially—by a factor of 2.5. Overall, the central mass increase seem to be better reproduced by the modification introduced by Gnedin et al. (2004). The standard formula overestimates the central density, which agrees with the results of Gnedin et al. for cosmological halos.

Figure 4 shows the dark matter density profiles of models D_{cs} and K_{cb} (cold and disk-dominated models) and models K_{hb} and D_{cb} (hot and dark-dominated models). The adiabatic density profiles are computed by differentiating the corresponding mass
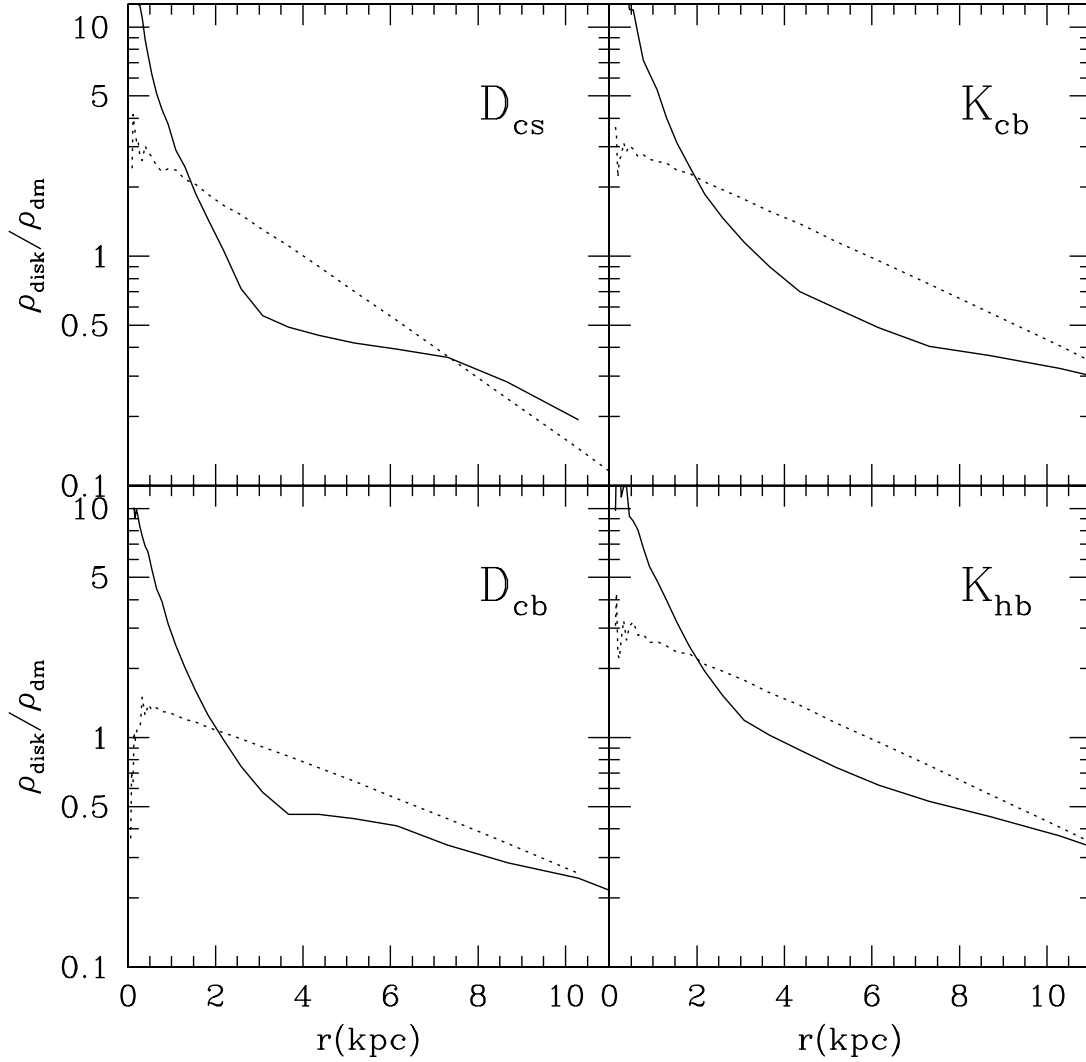
Fig. 5.—Disk-to-DM ratio for models D_{cb}, K_{hb}, D_{cs}, and K_{cb}. The dotted curves represent the initial models. The final models are shown with solid curves. The increase in the disk central density is produced at the expense of the density in middle region. This effect is slightly more pronounced in the cold- and disk-dominated models D_{cs} and K_{cb}. [*See the electronic edition of the Journal for a color version of this figure.*]

profiles. We decided to show only the predictions by the adiabatic contraction formalism developed by Gnedin et al. (2004) because the standard adiabatic contraction formula does not produce better results. In order to reduce the shot noise, we average five consecutive snapshots in both final and initial profiles. As was already noted in the cumulative mass profiles (Fig. 3), the increase in the inner halo density is higher in disk-dominated and cold models (D_{cs} vs. D_{cb} or K_{cb} vs. K_{hb}). The inner slope is steeper than $\gamma = -1$ in all models except in model D_{cb}. The rather flat inner density slope of model D_{cb} (*see bottom left panel*) is related to the fact that the inner density profile of the stellar disk is also flat in this model.

To summarize, we find that the increase in the halo central density is compatible with the adiabatic compression. In particular, we find that the inner halo density increase is better reproduced by the formalism developed by Gnedin et al. (2004). In models in which this density increase is smaller (e.g., model D_{cb}), the adiabatic compression tends to overestimate the DM density in the central region.

Figure 5 gives additional information on the changes in the dark matter. It shows the ratio of the disk to the halo densities as a function of radius. At the end of the evolution in all models

the stellar component strongly dominates the central ~ 1 kpc region.

5. SHAPE OF THE DARK MATTER HALO

The ellipticity of different components (DM or stellar) as well as the directions of the principal axes are determined by iteratively diagonalizing the inertia tensor. We start by finding the tensor of inertia for all particles inside a spherical shell of given radius R. We can take either stellar or DM particles depending on what component we study. We then find principal semiaxes $a > b > c$ and angles of the tensor. In the next iteration, we find the modified inertia tensor I_{ij} for particles inside an elliptical shell with the orientation given by the inertia tensor on the previous iteration and with the semiaxes R, $(b/a)R$, and $(c/a)R$:

$$I_{ij} = \sum_k \frac{x_{i,k} x_{j,k}}{d_k^2}, \qquad (8)$$

$$d_k^2 \equiv x_{1,k}^2 + \frac{x_{2,k}^2}{q^2} + \frac{x_{3,k}^2}{s^2}, \qquad (9)$$
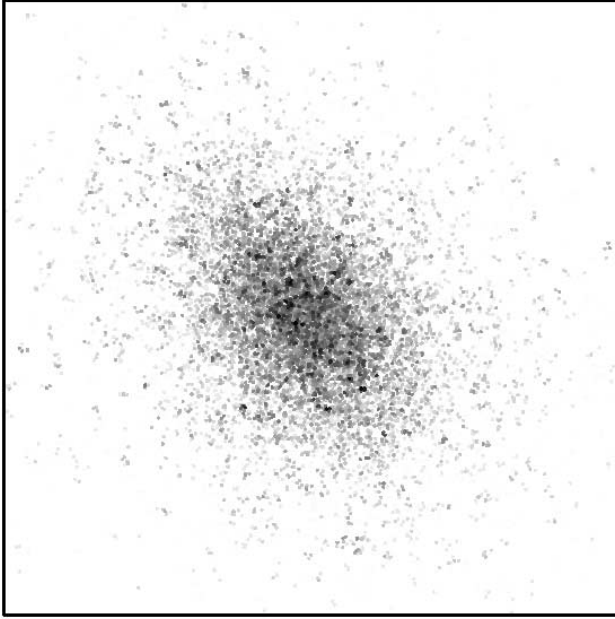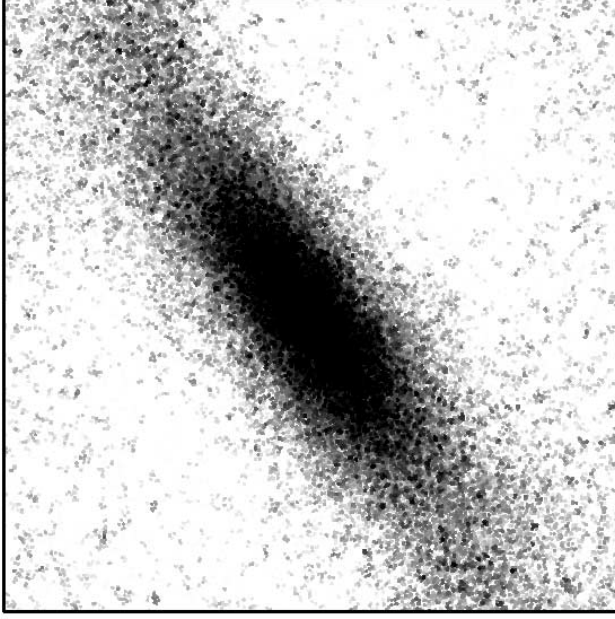
$$q \equiv b/a, \ s \equiv c/a. \qquad (10)$$

Fig. 7.—Flattening $f \equiv 1 - c/a$ (*solid curve*) and ellipticity in the plane of the disk $\epsilon_D \equiv 1 - b/a$ (*dashed curve*) of the DM distribution, where a, b, and c are the major, intermediate, and the minor axes. We show models D_{cs} (*left*) and D_{cb} (*right*) at the last measured epoch $t \sim 6$ Gyr. The differences between the weak bar model D_{cs} and the strong bar model D_{cb} are clearly seen. [*See the electronic edition of the Journal for a color version of this figure.*]

in width. As expected, the minor axis lies almost perpendicular to the plane of the disk.

Figure 6 highlights the presence of the stellar and the DM bars in model D_{cb}, which has a strong bar. The stellar bar shown in the top panel has a rectangular-like shape, while the halo bar shown in bottom panel is more round. Note that both bars have their major axes pointing to approximately the same direction.

Figure 7 shows the flattening, $f \equiv 1 - s = 1 - c/a$, and the ellipticity of the dark matter in the plane defined by major and intermediate axes, $\epsilon_D \equiv 1 - q = 1 - b/a$, as a function of distance R to the center for models D_{cs} and D_{cb} at the last simulated epoch ~ 6 Gyr (hereafter f and ϵ_D are referred to as ellipticities). The plot shows that DM bars are typically triaxial. In models with a strong stellar bar, as in model D_{cb}, the DM bar can be more prolate than oblate. As shown in Figure 7, axial ratios increase with increasing radius (thus, the system is getting more round). For example, at 15 kpc models D_{cs} and D_{cb} show comparable

Fig. 6.—Distribution of disk (*top*) and dark matter particles (*bottom*) inside a box of 10 kpc across for model D_{cb} at $t \sim 6$ Gyr. The figure shows the face-on projection of the particles. The halo bar is clearly seen in the bottom panel. To improve the contrast, we have color-coded particles on a gray scale according to their local three-dimensional density (a `pgplot` code kindly provided by A. Kravtsov) and plotted only DM particles with the z-component of velocity $|v_z| < 100$ km s^{-1}.

Here the sum is taken over all particles inside the elliptical shell. In equations (8)–(10) $x_{i,k}$ ($i = 1, 2,$ and 3) are the coordinates of the particle k with respect to the center of the disk-halo system and d_k is the elliptical distance; s is the short-to-long axis ratio, and q is the intermediate-to-long axis ratio. The center of the system is found iteratively as the center of mass of a sphere containing maximum mass. The radius of the sphere is equal to the disk scale length R_d. The elliptical bins are chosen so that they have roughly the same number of particles and are less than 1 kpc
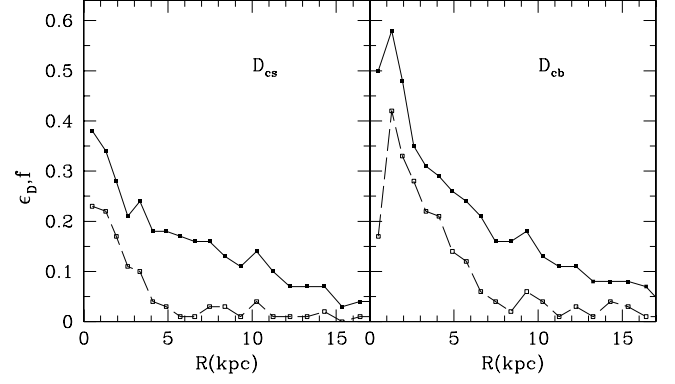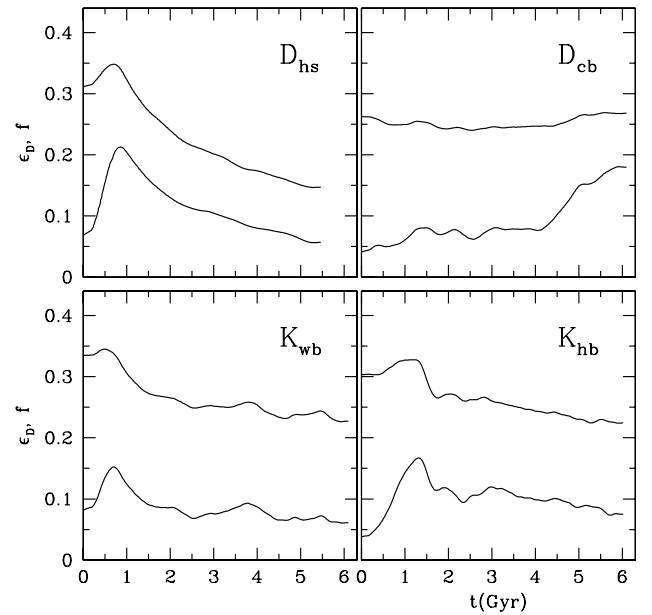

Fig. 8.—Evolution of the DM ellipticities f (*top*) and ϵ_D (*bottom*) for four of our seven models. Ellipticities are evaluated at $r = R_d$, where R_d is the scale length of the corresponding model. [*See the electronic edition of the Journal for a color version of this figure.*]
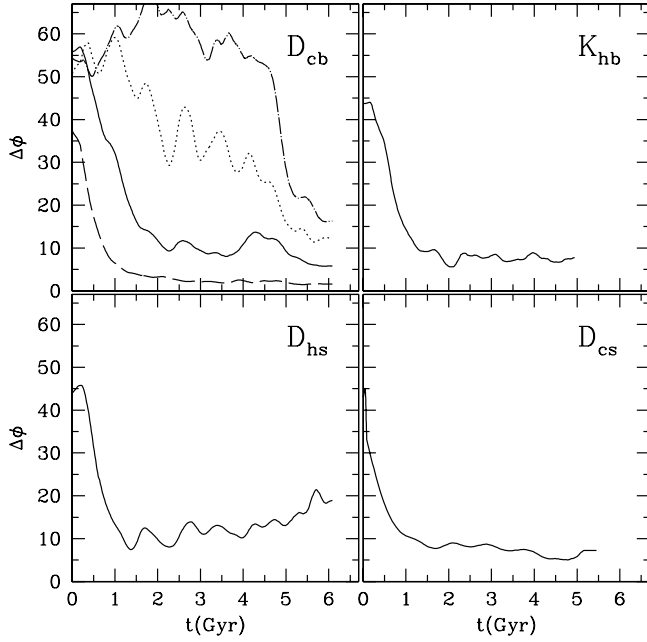
Fig. 9.—Evolution of the phase difference between the stellar and the DM bars for four models at radius R_d (*solid curves*). For the strong bar model D_{cb} we also show the evolution of $\Delta\phi$ at other radii: $R = 0.5R_d$ (*dashed curve*), $1.5R_d$ (*dotted line*), and $2.0R_d$ (*dot-dashed curve*). The curves show that the phase difference is an increasing function of radius. Interestingly, the two periods in which $\Delta\phi$ drops (*solid and dot-dashed curves*) seem to coincide with the two periods in which a higher angular momentum loss rate is observed. At $R = R_d$ an alignment within $10°$ is observed in models that end up with strong and moderate stellar bars by the end of evolution. [*See the electronic edition of the Journal for a color version of this figure.*]

small ellipticities, while in the central regions the models have very different flattening.

Evolution of the DM ellipticities with time is shown in Figure 8. By comparing Figure 2 with Figure 8 we find similarities of behavior of the stellar bar amplitude with the evolution of DM bar ellipticity. Indeed, in models D_{hs} and K_{hb} the maximum in the stellar bar amplitude A_2 and the maximum of ellipticity ϵ_D are reached at approximately the same time. Moreover, in model D_{cb} the second period of the stellar bar growth is mirrored by an increase in the ellipticity of the DM bar. The gradual decline of A_2 in models D_{hs}, K_{cb}, and to a smaller degree in model K_{hb} is imitated by a decline in ϵ_D.

At the onset of the evolution, the sole presence of the disk produces a flattening of the DM halo in the central region. The subsequent evolution of the shape of the DM halo depends on the model. For example, in model D_{hs} the ellipticities first increase as the stellar bar growths. Then they decline maintaining a figure of constant triaxiality. On the other hand, in model D_{cb} the flattening f stays approximately constant after the initial period of stellar bar growth. This latter effect, along with the growth of ellipticity ϵ_D, produces in models D_{cb} and A_{wb} (not shown in the figure) a near prolate central DM halo by the end of the evolution. In summary, Figures 2, 6, and 8 show a clear indication of the disk-halo coupling (for details see § 6).

5.1. *Bar Orientation*

We use the position angle (P.A.) of the stellar bar and the orientation of the DM bar measured at $r = R_d$ to build the evolution of the bars' phase difference, $\Delta\phi$. Figure 9 shows the evolution of $\Delta\phi$ for four of our seven models. At R_d the bar alignment within $\sim10°$ is reached soon after the initial stellar bar
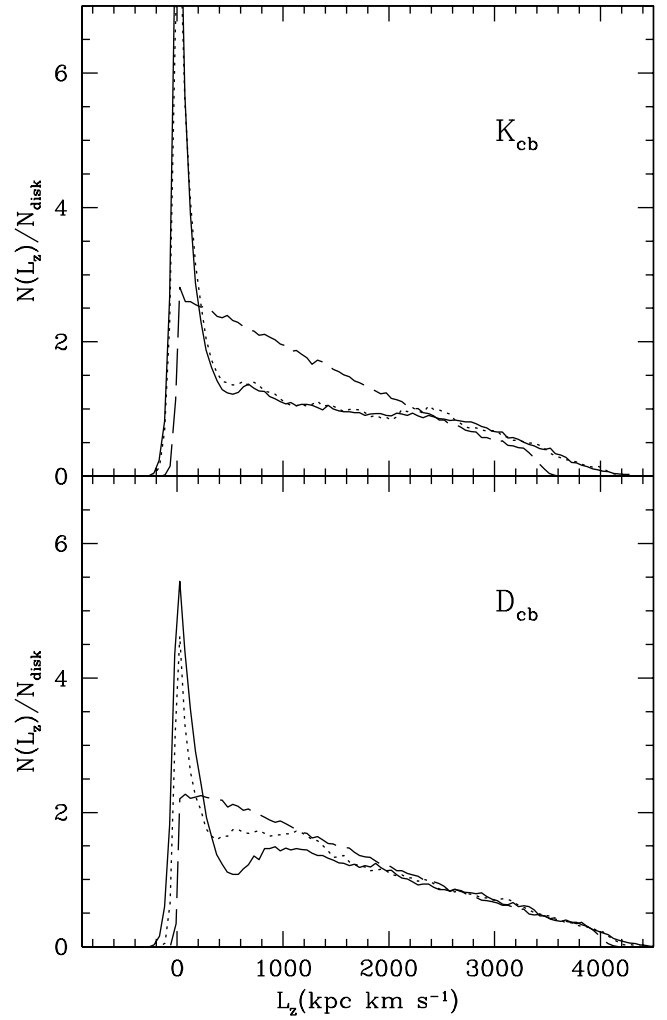

Fig. 10.—Distribution of the *z*-component of the angular momentum of the stellar particles for models K_{cb} (*top*) and D_{cb} (*bottom*), shown at different epochs: initial (*long-dashed curve*), at $t \sim 1.6$ Gyr (*dotted curve*), and at $t \sim 5$ Gyr (*solid curve*). Particles with low (high) angular momentum are preferentially at small (large) radii. The distributions are qualitatively similar to those shown by Valenzuela & Klypin (2003; see their Fig. 12): a peak at low L_z, which corresponds to the bar, a valley at intermediate values of L_z, and an excess of particles with very large angular momentum. Note that in the weak bar model K_{cb} the distribution barely changes for the period 1.6–5.0 Gyr, while the redistribution of angular momentum continues in the strong bar model D_{cb}. [*See the electronic edition of the Journal for a color version of this figure.*]

growth (the DM bar trails the stellar bar). The start of the second period of stellar bar growth in model D_{cb} coincides with a small increase in $\Delta\phi$—the DM bar gets a larger lag. This renewed disalignment quickly dies out, and the bars again rotate in phase. More significantly, this second period coincides with the period of a strong influence of the stellar bar on the halo, which is reflected in the more extended bar alignment (see Fig. 9, *top left panel, dot-dashed curve*). These two periods of stellar bar growth and bar alignment also coincide with the two periods in which a higher angular momentum loss rate is observed (see Figs. 11 and 12).

The phase difference $\Delta\phi$ of the bars is related to the torque experienced by the stellar bar: the torque slows down the bar pattern speed. In model A_{wb} (see Fig. 2) the oscillations seen in Ω_p, and to some degree also in A_2, are very likely coming from the strong oscillations seen in $\Delta\phi$ in this model. The onset of the late period of bar growth coincides with a decline of about $40°$ in $\Delta\phi$:
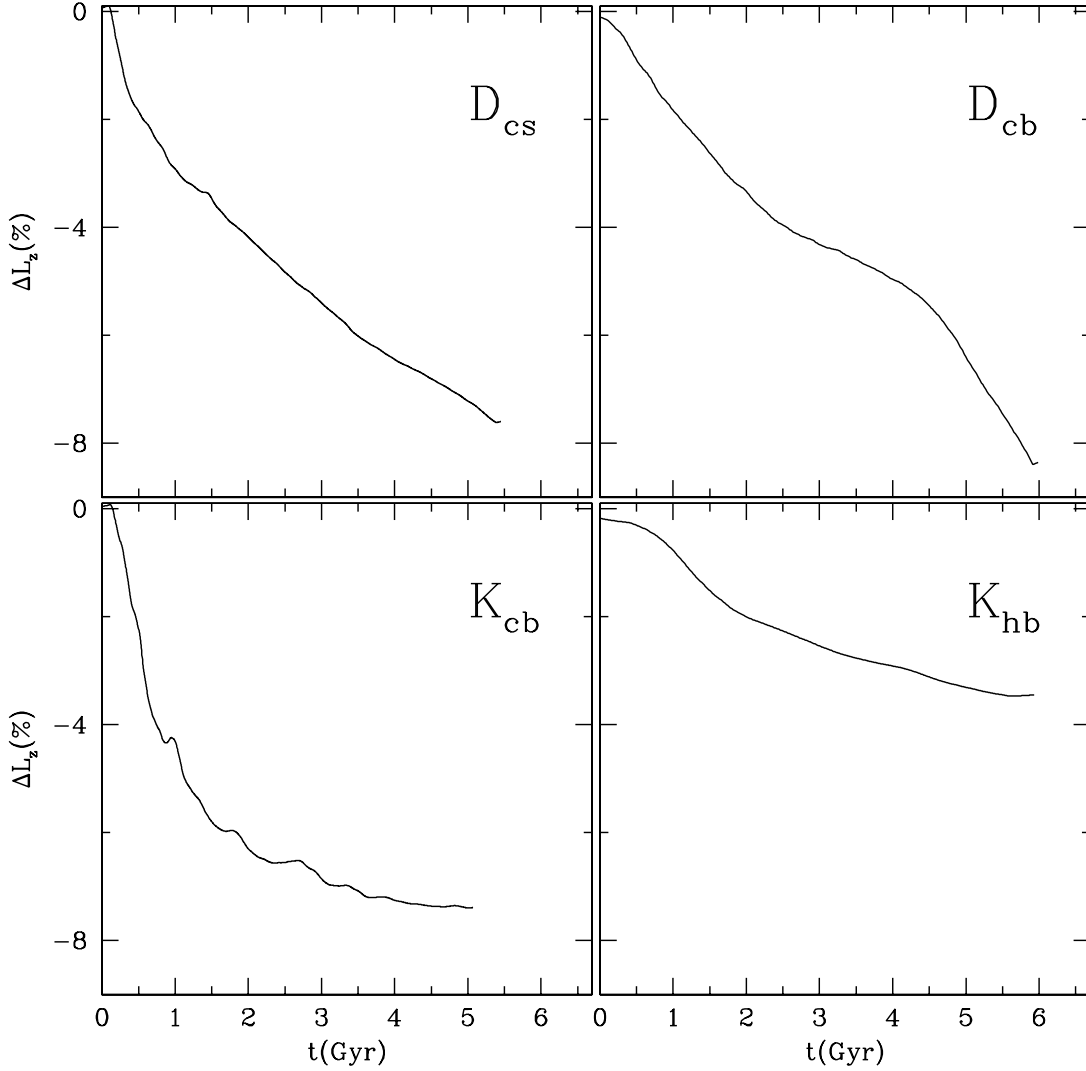
Fig. 11.—Evolution of the disk angular momentum for four models. We show two models, D_{cb} and D_{cs}, that end up with strong bars at the end of the simulated period and two other models, K_{cb} and K_{hb}. Model D_{cb} presents an inflection point or zone, in which the rate of angular loss changes its decreasing trend to an increasing one. This time coincides with the second period of bar growth.

the $m = 2$ halo structure is quickly reoriented toward the direction of the stellar bar. Moreover, the rapid growth of the stellar bar in model D_{cs} (see Fig. 2) produces a DM bar that very soon aligns with the stellar bar.

6. ANGULAR MOMENTUM

The bar growth is intimately related to its slowing down. The rate of change of Ω_p correlates with the initial conditions. For example, the A_2 maximum is reached earlier in disk-dominated models (cf. D_{cs} with D_{cb}), or in cold disk models (K_{cb} vs. K_{hb}). During the bar braking, the angular momentum is transferred from the disk to the halo.

Figure 10 shows the distribution of the disk L_z component of the angular momentum for two models, the strong bar model D_{cb} and the cold model K_{cb}, one of the models with a strong decline in bar amplitude. We show the distribution of L_z at three moments of time: initial, at $\sim$1.6 Gyr, and at $\sim$5 Gyr. Disk particles in the intermediate-L_z zone lose angular momentum and move to the low-L_z region close to the center. At the same time, the number of particles with very high-L_z, which are preferentially at larger radii, increases. Note that the number of intermediate-L_z

particles in model K_{cb} barely changes from $t \sim 1.6$ to $\sim$5 Gyr, while this is not the case for model D_{cb}. This behavior is compatible with the much higher angular momentum loss by model D_{cb} during this period of time shown in Figure 11.

The evolution of the relative change in L_z is plotted in Figure 11, where we show four models: three cold models D_{cs}, K_{cb}, and D_{cb} and one hot and disk-dominated model K_{hb}. In the K_{cb} model, the amount of angular momentum lost by the disk is very small during the declining phase of the bar amplitude. Moreover, the disk in models D_{cs} and D_{cb} has lost, by the end of the evolution, about 10% of its angular momentum.

It is interesting to estimate what fraction of the torque experienced by the stellar disk is coming from the interaction between the dark matter bar and the stellar bar. Unfortunately, the torque is difficult to estimate accurately because of the complex structure of the bars: the bars change shape, mass, and length as the evolution proceeds. Still, we can start with simple scaling relations. The torque should be proportional to the masses and radii of the bars. It is also proportional to the strength of the bars, which can be measured by ellipticities $q = 1 - b/a$, where a and b are the major and minor semiaxes in the plane of the disk. The angle
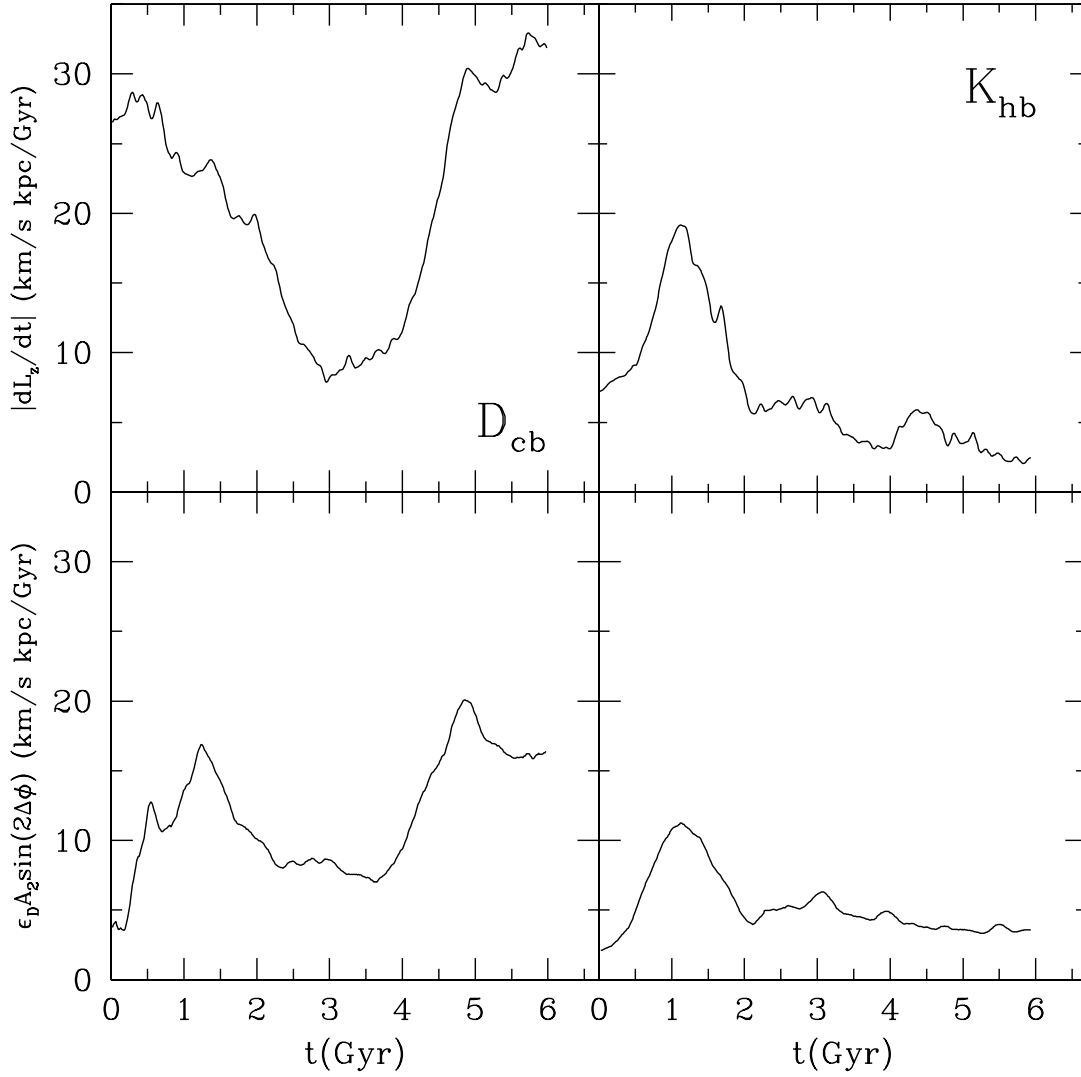
Fig. 12.—Top panels show the specific torque dL_z/dt experienced by the stellar component in models $D_{\rm cb}$ and $K_{\rm hb}$ with a strong and a moderate stellar bar, respectively. The bottom panels show the evolution of an estimate of the torque due only to interaction between the stellar and the dark matter bars: $\tau = \epsilon_D A_2 \sin(2\Delta\phi)$, where ϵ_D, A_2, and $\Delta\phi$ are the ellipticity of the halo bar, the amplitude of the stellar bar, and the lag angle, respectively. Torque dL_z/dt is reasonably well reproduced by interaction between the bars during most of evolution.

$\Delta\phi$ between the bars also affects the torque. From the geometry of the problem, we expect that the torque is zero, when the angle is either zero or 90°.

In order to test the scaling relations, we estimate the torque between two elliptical-shaped objects that roughly mimic our bars. The boundary of each object is assumed to be a triaxial ellipsoid with semiaxes $a > b > c$: $(x/a)^2 + (y/b)^2 + (z/c)^2 = 1$. For the ellipsoid representing the stellar bar we use $c/a = 0.1$. For the dark matter bar $c/a = 0.5$. The other axial ratio b/a was varied for both ellipsoids to test its effect on the torque. We also varied the angle between the bars. The density was chosen to fall exponentially with the distance mimicking the decline of the density in bars measured in our N-body models. The ellipsoid representing the dark matter bar was 2 times shorter than the stellar bar. We use the Monte Carlo method to estimate the torque between the ellipsoids. We find that the torque τ between the ellipsoids scales as $\tau \propto \epsilon_{\rm DM}\epsilon_{\rm stellar} \sin(2\Delta\phi)$, which is what one naively expects. Once the parameters of the ellipsoids are fixed, the model also provides absolute value of the torque. We used parameters of bars in model $D_{\rm cb}$ at 3 Gyr to roughly estimate the torque. Indeed, we find that the expected torque between the bars

and the measured torque in model $D_{\rm cb}$ are quite close (within 30%). This is reassuring, but unfortunately, it is difficult to press this issue because matching the masses and the density distributions with bars in real simulations is difficult. Instead, we decided to use only the scaling relation for the torque. In this case we use the amplitude of the stellar bar A_2 as a measure of the bar strength. The amplitude of the expected torque is fixed to have the observed value at one moment in our models: at 3 Gyr.

We tested three of our models. In Figure 12 we show the rate of angular momentum loss of the disk as a function of time (*top panels*) for models $D_{\rm cb}$ and $K_{\rm hb}$. In the bottom panels we show the evolution of the quantity $\tau = A_2\epsilon_D \sin(2\Delta\phi)$ measured at $r = R_d$ and normalized at 3 Gyr. Parameters A_2, ϵ_D, and $\Delta\phi$ are the amplitude of the disk bar, the ellipticity of the DM bar, and the phase between the bars, respectively, introduced in previous sections. With the exception of the first ~1 Gyr (model $D_{\rm cb}$), the observed torque dL_z/dt and the estimated torque between the bars are remarkably similar. After the initial stage, at $t \approx$ 1–2.5 Gyr the torque declines. The second growth of the stellar bar at about 4 Gyr in model $D_{\rm cb}$ produces an increase in dL_z/dt at later epochs.

We also find an agreement between the measured and estimated torques for other models. We note that none of the quantities in the estimate of τ can *separately* explain even qualitatively the time behavior of dL_z/dt. Indeed, the decline in the torque from 1.5 to 3 Gyr is mostly due to a decrease of the angle between the bars. Yet the steep increase in dL_z/dt at 4 Gyr in model D_{cb} is not related with the angle: the angle keeps decreasing. The increase is mostly due to the growth of the amplitude of the stellar bar, which is accompanied by an increase in the ellipticity of the dark matter bar (see Fig. 8). In spite of general agreement of the torques, there are some deviations. At early stages ($t < 1$ Gyr) the scaled value of τ is too small compared with the measured torque in the cold model D_{cb}. This is hardly surprising because the disk in this model develops instabilities very quickly. In addition, it was difficult to set the very central ~ 200 pc of the disk initially in equilibrium. Thus, irregular nonaxisymmetric waves are present almost from the very beginning. These waves result in $\sim 1\%$–2% loss of the disk angular momentum. At around 0.1 Gyr the disk develops strong spiral arms, which likely account for a large fraction of the torque at that time. As the spiral arms die and the bar grows, the torque starts to be dominated by the interaction between the dark matter and the stellar bars, and the τ approximation works better.

Judging by the similarities between $dL_z/dt(t)$ and $\tau(t)$, we find it plausible that the torque between the stellar and the DM bars is responsible for a large fraction of angular momentum transfer between the disk and the dark matter.

7. DISCUSSION AND CONCLUSIONS

Like many other groups in the field (e.g., Athanassoula 2005a, 2005b; Shen & Sellwood 2004; Debattista & Sellwood 1998) we find that our disk models develop strong, moderate, and weak bars. They show what seems to be a generic feature of bar simulations: the growth in their amplitude is accompanied with a decrease in their pattern speed. The role that the halo plays in this phenomenon appears to be crucial. The dark matter ellipsoidal figure, the halo bar, that arises due to the presence of the disk and stellar bar exerts a torque on the stellar bar that slows it down. It is thus not surprising to find that the first period of bar growth (the only one in some models) coincides with a decline in the phase difference between the disk and the halo bar. Interestingly, an opposite trend seems to exist as well: bars rotate faster as they weaken. This is clearly seen in models K_{cb} and D_{hs}.

Disk particles located in the middle 2–8 kpc region transfer angular momentum to the halo and to the outer disk region. In particular, this effect would explain the increase of the central stellar density seen, for example, in Figures 8–9 of Valenzuela & Klypin (2003; see also Avila-Reese et al. 2005). We have seen in § 4 that this disk density increase is accompanied by a corresponding central halo density increase. We apply the adiabatic contraction formalism to study whether the compression of the halo could be modeled by it. We find that the modified formalism by Gnedin et al. (2004) reproduces relatively well the inner density growth, whereas the standard formula typically overestimates the density increase.

We compute the ellipticities of the halo bar in a plane parallel, ϵ_D, and perpendicular, f, to the disk plane. The ellipticities decrease and the halo bar becomes more spherical as the radius increases. In some models, after an initial increase, the flatness stays roughly constant or decreases during the disk evolution. On the other hand, in models with strong bars like model D_{cb}, the ellipticity ϵ_D has a second period of increase, which agrees with the second growth period of the stellar bar. As a result, at the end of the evolution the inner dark matter halo ends up with a near prolate-like shape. Our results roughly agree with those mentioned in Athanassoula (2005a, 2005b).

In all models, the inner halo ($r \lesssim 5$ kpc) is flattened, with the minor axis pointing perpendicular to the disk plane. The alignment of the minor axis with the disk axis is compatible with the results of Bailin et al. (2005). In cosmological simulations of disk galaxy formation Bailin et al. (2005) find that the inner halo ($r \lesssim 0.1 R_{vir}$) orients its minor axis parallel to the disk axis, regardless of the orientation of the outer halo. As they explain, the misalignment between the two halo regions should be taken into account when modeling tidal streams in the halos of disk galaxies.

Long et al. (1992) found that the presence of a stellar bar in the center of our Galaxy does not strongly affect the destruction rates of globular clusters. The results of Long et al. (1992) or of similar studies (e.g., Pichardo et al. 2004) might change in light of our findings: halo bars could enhance the dynamical effect of bars on globular clusters distribution.

We use the same method of the tensor of inertia to study the evolution with time of the orientation of the halo bar relative to the disk bar. In all models, an alignment within $\sim 10°$ is obtained after the initial bar growth. In some models, for example, model K_{hb}, the bars stay aligned during the whole evolution. It is interesting to see that in model D_{cb} the periods of alignment roughly agree with the two periods of stellar bar growth. In turn, the periods of bar growth are also the periods of higher angular momentum loss rate.

As in Valenzuela & Klypin (2003), we also find that the angular momentum transfer from the disk to the halo is rather modest: it is less than 10%. As it was shown by Valenzuela & Klypin, this is partly due to the fact that a significant fraction of the disk angular momentum is not lost but redistributed: outer regions absorb part of the angular momentum of intermediate regions.

REFERENCES

Athanassoula, E. 1996, in IAU Colloq. 157, Barred Galaxies, ed. R. Buta, D. A. Crocker, & B. G. Elmegreen (ASP Conf. Ser. 91; San Francisco: ASP), 309
———. 2002, ApJ, 569, L83
———. 2003, MNRAS, 341, 1179
———. 2005a, Celest. Mech. Dyn. Astron., 91, 9
———. 2005b, in Nonlinear Dynamics in Astronomy and Physics, ed. S. T. Gottesman, J.-R. Buchler, & M. E. Mahon (Boston: Blackwell), 168
Athanassoula, E., & Misiriotis, A. 2002, MNRAS, 330, 35
Avila-Reese, V., Carrillo, A., Valenzuela, O., & Klypin, A. 2005, MNRAS, 361, 997

Bailin, J., et al. 2005, ApJ, 627, L17
Binney, J., & Tremaine, S. 1987, Galactic Dynamics (Princeton: Princeton Univ. Press)
Blumenthal, G. R., Faber, S. M., Flores, R., & Primack, J. R. 1986, ApJ, 301, 27
Bullock, J. S., Kolatt, T. S., Sigad, Y., Somerville, R. S., Kravtsov, A. V., Klypin, A. A., Primack, J. R., & Dekel, A. 2001, MNRAS, 321, 559
Combes, F., Debbasch, F., Friedli, D., & Pfenniger, D. 1990, A&A, 233, 82
Debattista, V. P., & Sellwood, J. A. 1998, ApJ, 493, L5
———. 2000, ApJ, 543, 704

de Blok, W. J. G., Bosma, A., & McGaugh, S. 2003, MNRAS, 340, 657
Gnedin, O. Y., Kravtsov, A. V., Klypin, A. A., & Nagai, D. 2004, ApJ, 616, 16
Hernquist, L. 1993, ApJS, 86, 389
Hernquist, L., & Weinberg, M. D. 1992, ApJ, 400, 80
Holley-Bockelmann, K., Weinberg, M. D., & Katz, N. 2005, MNRAS, 363, 991
Ibata, R., Lewis, G. F., Irwin, M., Totten, E., & Quinn, T. 2001, ApJ, 551, 294
Jing, Y. P., & Suto, Y. 2002, ApJ, 574, 538
Kazantzidis, S., Kravtsov, A. V., Zentner, A. R., Allgood, B., Nagai, D., & Moore, B. 2004, ApJ, 611, L73
Klypin, A. A., Zhao, H., & Somerville, R. 2002, ApJ, 573, 597
Kravtsov, A. V., Klypin, A. A., & Khokhlov, A. M. 1997, ApJS, 111, 73
Little, B., & Carlberg, R. G. 1991, MNRAS, 250, 161
Long, K., Ostriker, J. P., & Aguilar, L. 1992, ApJ, 388, 362
Navarro, J. F., Frenk, C. S., & White, S. D. M. 1997, ApJ, 490, 493

O'Neill, J. K., & Dubinski, J. 2003, MNRAS, 346, 251
Pichardo, B., Martos, M., & Moreno, E. 2004, ApJ, 609, 144
Rhee, G., Valenzuela, O., Klypin, A., Holtzman, J., & Moorthy, B. 2004, ApJ, 617, 1059
Ryden, B. S., & Gunn, J. E. 1987, ApJ, 318, 15
Sellwood, J. A. 2003, ApJ, 587, 638
Shen, J., & Sellwood, J. A. 2004, ApJ, 604, 614
Springel, V., Yoshida, N., & White, S. D. M. 2001, NewA, 6, 79
Swaters, R. A., Madore, B. F., van den Bosch, F. C., & Balcells, M. 2003, ApJ, 583, 732
Valenzuela, O., & Klypin, A. 2003, MNRAS, 345, 406
Weinberg, M. D. 1985, MNRAS, 213, 451
Weinberg, M. D., & Katz, N. 2005, preprint (astro-ph/0508166)
Weldrake, D. T. F., de Blok, W. J. G., & Walter, F. 2003, MNRAS, 340, 12